

Loss characterization methodology for soft magnetic nano-crystalline tape materials in coupled inductors

David Bohne, Valentin Wagner, Patrick Deck, Christian P. Dick

TH KÖLN

Betzdorfer Straße 2

50679 Cologne, Germany

Phone: +49 221 8275-2262

Email: dbohne@th-koeln.de

URL: <http://www.th-koeln.de/lea>

Acknowledgments

The GaN-HighPower project on which this paper is based was funded by the German Federal Ministry for Economic Affairs and Climate Action under grant number 03EE1111F. The author is responsible for the content of this publication.

Keywords

«loss characterization», «soft magnetic material», «four-wire measurement», «two- winding»,
«coupled inductors»

Abstract

In this paper a four-wire magnetic core loss measurement test bench for waveforms typical for two-phase Coupled Inductors is presented. A low permeability nano-crystalline ribbon material is investigated. The advantage of the new test bench is its low measurement time of seconds for multiple operating points at good accuracy. Due to the improvements in preventing disturbances, the measurements are reliable and reproducible.

Introduction

General description

A big challenge in the improvement of power converters is the reduction of volume and weight. Cores used in filter inductors have a major impact on the power density. In [1] it is shown, that with inversely wound Coupled Inductors (CI) the core volume can be significantly reduced in N-phase interleaved converters. For an optimal design of CI, losses in deployed cores made of soft magnetic materials play an important role. These losses depend on temperature, AC flux frequency, DC bias, waveform and amplitude of the flux [2] [3]. Most accurate calorimetric methods for determining losses in magnetics are very time-consuming [4], this problem should be addressed with the developed test bench.

With power converters and their magnetic components improved to high power densities, core materials developed as well. In addition to low hysteresis and eddy current losses, the investigated nano-crystalline tape material features high saturation flux densities and low permeabilities [5]. These characteristics make it suitable for high frequency and high efficiency applications [6][7].

In this paper, a loss characterization methodology for the nano-crystalline tape material VITROPERM® 850FF [8] is introduced for special flux waveforms, which occur in the coupling and leakage path of coupled tape-wound cores. Fig. 1 depicts exemplary flux waveforms for such special setups as presented in [1].

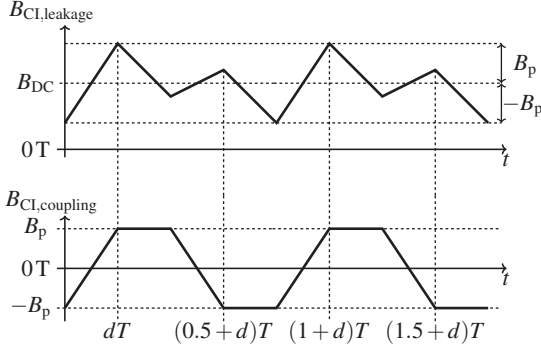


Fig. 1: Flux waveforms in two-phase CI for leakage and coupling path corresponding to current $i_{\text{pri}}(t)$ in two-winding method

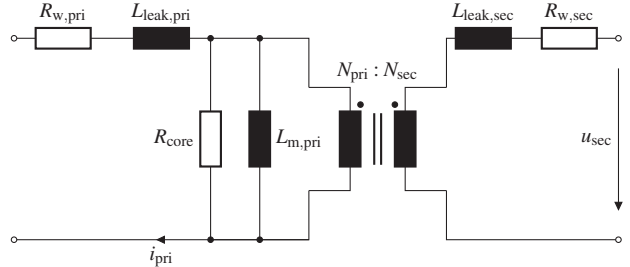


Fig. 2: Equivalent circuit of core with primary and secondary side winding (leakage inductances $L_{\text{leak},\text{pri}}$, $L_{\text{leak},\text{sec}}$, winding resistances $R_{w,\text{pri}}$, $R_{w,\text{sec}}$, representative resistance for core losses R_{core})

Two-winding / four-wire method

For fast loss measurement, the electrical two-winding/four-wire method is widely used [9] [10]. Based on the equivalent circuit of the Device Under Test (DUT) (Fig. 2), core losses are represented by the resistor R_{Core} [11]. Loss measurement requires the primary side to be excited with waveforms for which losses are to be characterized. By measuring the current on the primary side and the voltage on the unloaded secondary side, core losses can be calculated with following equation:

$$P_{\text{Fe}} = \frac{N_{\text{pri}}}{N_{\text{sec}} T} \int_0^T u_{\text{sec}}(t) i_{\text{pri}}(t) dt \quad (1)$$

This method allows hysteresis and eddy current losses to be measured separately from winding losses [3]. However, it suffers from parasitic effects in sensing the primary current as core losses are very sensitive to phase discrepancies between the measured signals [10] [12] [13]. With

$$P_{\text{Fe}} \sim \cos(\phi_{\text{actual}} + \phi_{\text{error}}) \quad (2)$$

this problem can be very severe, especially towards high frequencies.

Another common way to measure core losses is the thermal approach by means of a calorimeter [14], which doesn't face the challenges mentioned for high frequencies. The thermal approach is very time-consuming and with increasing frequency it becomes hard to distinguish core from winding losses [4] [2]. Compared to the two-winding method, the thermal approach is not preferred.

Developed test bench

The equivalent circuit of the developed test bench can be seen in Fig. 3. The waveforms shown in Fig. 1 are generated by two half bridges HB3 and HB4, while the supply voltages are provided by HB1 and HB2. A DC filter realized by a large capacitance ($C_f = 750 \mu\text{F}$) is placed at the output to block any DC currents during measurement. This setup can be extended by placing a third winding on the DUT to superpose AC fluxes with DC bias. The switching patterns of HB3 and HB4 and the resulting voltage $u_{\text{DUT}}(t)$ and current $i_{\text{pri}}(t)$ are shown in Fig. 4 for leakage path and in Fig. 5 for coupling path waveforms in two-phase CI.

A coaxial shunt resistor R_{shunt} with very low ESL ($L_{\text{ESL}} \approx 35 \text{ pH}$) is chosen to measure the primary current $i_{\text{pri}}(t)$ and to avoid big errors caused by the phase discrepancy (2). The voltages $u_{\text{shunt}}(t)$ and $u_{\text{sec}}(t)$ are measured with differential probes.

The isolated measurement for $u_{\text{shunt}}(t)$ in Fig. 3 experiences interferences caused by common mode voltages, since the coupling capacitance to ground potential of the differential probe is much smaller compared to the coupling capacitance of DC sources ($C_{\text{CM,probe}}$ and $C_{\text{CM,source}}$ in Fig. 6).

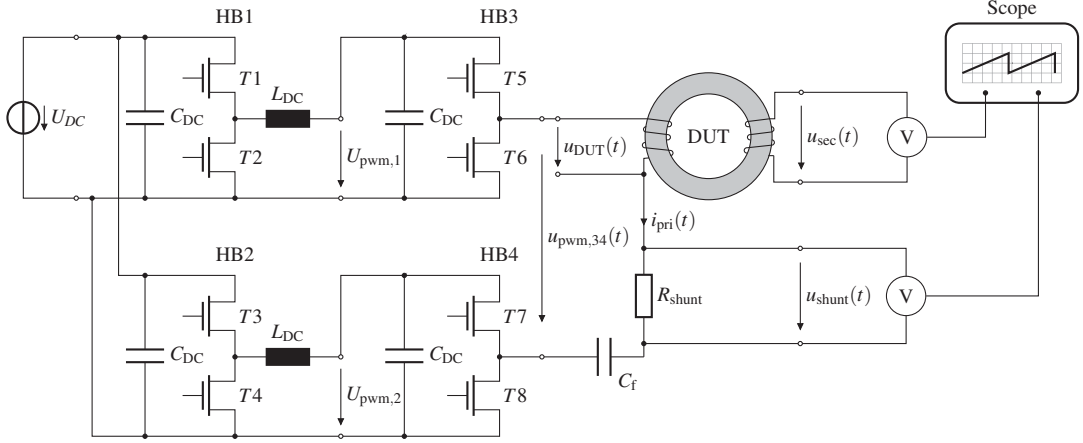


Fig. 3: Equivalent circuit of the developed test bench

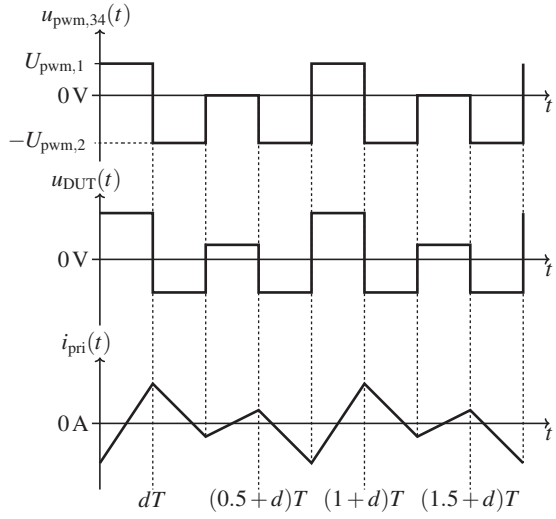


Fig. 4: Switchting pattern for the leakage path waveform in two-phase CI, $\bar{u}_{\text{DUT}} = 0 \text{ V}$

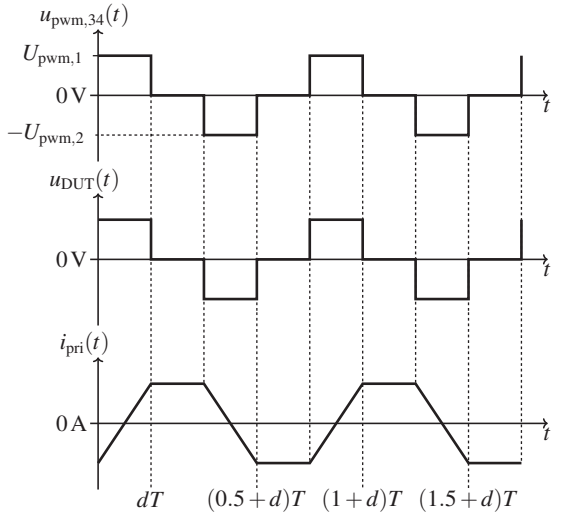


Fig. 5: Switchting pattern for the coupling path waveform in two-phase CI, $\bar{u}_{\text{DUT}} = 0 \text{ V}$

Grounding the shunt resistor leads to unsymmetrical common mode currents, resulting in an additional voltage over the shunt and thus, distorts the measurement. Without grounding the setup near the shunt resistor, unsymmetrical common mode voltages influence the measurement as well and prevent using higher measurement voltages since the probes used can not handle more than $U_{\text{CM},\text{max}} = 60 \text{ V}$.

Various arrangements are able to suppress common mode currents despite grounding the setup on the primary and secondary side of the DUT. A common mode choke is placed in front of the shunt resistor and the output design is adapted by adding a second DC filter C_f and inductance L_f to achieve a symmetrical setup. Common mode currents are reduced even further by decoupling all power inputs from their supplies. This is done by opening relay contacts in each supply line during measurement. To store enough energy for one measurement, DC link capacitors are enlarged and a 12 V battery is placed at the logic power input as an auxiliary supply. The adapted test bench including the ground connections can be seen in Fig. 6.

To accelerate the measurement process, the scope and all half bridges are controlled by a PC performing all setups and calculations, including error analysis.

For each measurement, fifty periods of $u_{\text{shunt}}(t)$ and $u_{\text{sec}}(t)$ are recorded and losses are averaged to reduce the influence of noise. With the number of samples M for the amount of fifty periods recorded by the scope, the measured voltage $u_{\text{shunt}}(t)$ and the weight of the core m_{core} , the loss density $P_{\text{Fe,dens}}$ is

approximated by (3) based on (1) by the PC.

$$P_{\text{Fe,dens}} = \frac{N_{\text{pri}}}{N_{\text{sec}} R_{\text{shunt}} m_{\text{core}} M} \sum_{k=1}^M u_{\text{sec}}[k] u_{\text{shunt}}[k] \quad (3)$$

Each measurement determines the loss density $P_{\text{Fe,dens}}$ specified for the maximum flux B_p induced in the core, which can be calculated by integrating the time-dependent flux from $t_1 = dT/2$ to $t_2 = dT$ (Fig. 1). With the equivalent core cross sectional area A_{Fe} and the sampling time $T_S = 100\text{ps}$ this results in:

$$B_p = \frac{T_S}{A_{\text{Fe}} N_{\text{sec}}} \sum_{k=1}^{M'} u_{\text{sec}}[k] = \frac{\rho \pi (r_{\text{in}} + r_{\text{out}}) T_S}{m_{\text{core}} N_{\text{sec}}} \sum_{k=1}^{M'} u_{\text{sec}}[k] \quad (4)$$

with samples according to

$$B_p = \frac{1}{A_{\text{Fe}} N_{\text{sec}}} \int_{dT/2}^{dT} u_{\text{sec}}(t) dt \quad A_{\text{Fe}} = \frac{V_{\text{Fe}}}{l} \frac{V_{\text{Fe}} = \frac{m_{\text{core}}}{\rho}}{l = 2\pi \frac{r_{\text{in}} + r_{\text{out}}}{2}} \frac{m_{\text{core}}}{\rho \pi (r_{\text{in}} + r_{\text{out}})}$$

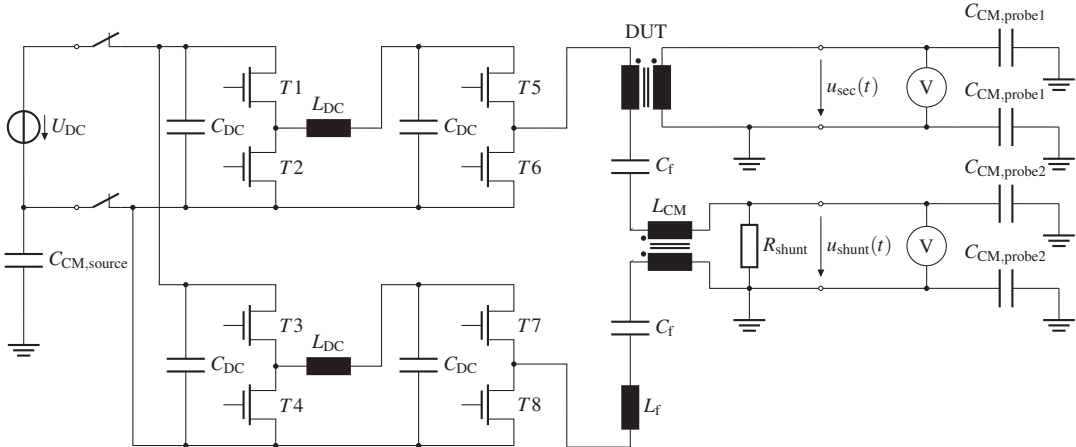


Fig. 6: Equivalent circuit of the extended test bench for common mode suppression

Error Analysis

Based on (3) and (4), various error sources need to be analyzed in this section. Due to non-sinusoidal waveforms, the error calculation is done by decomposing the two measured signals into their corresponding fourier series, neglecting the nonlinear dependence of core losses on both, flux and frequency. As can be seen in Fig. 12 later, more than 95 % of the total error can be explained with the proposed simplification based on the fourier decomposition. Thus, especially the share of the different loss contributors in Fig. 9 is valid in its main message. The remaining only 5 % difference of the losses in Fig. 12 mean that the calculated error bars have a very high confidence level. Therefore, this simplification is sufficiently accurate for error calculation and allows to derive the following calculations for sinusoidal waveforms.

Error sources

The total error is composed of following different sources:

1. weight m_{core}
2. value of shunt resistor R_{shunt}
3. amplitude and offset error in measured $u_{\text{shunt}}(t)/u_{\text{sec}}(t)$
4. phase ϕ_{actual}
5. radii $r_{\text{in}}/r_{\text{out}}$ of the DUT

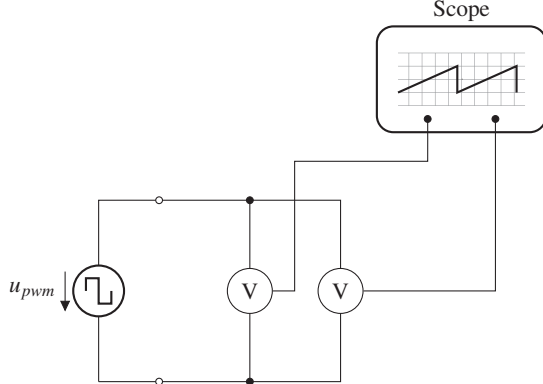


Fig. 7: Equivalent circuit of the mismatch determination between used probes

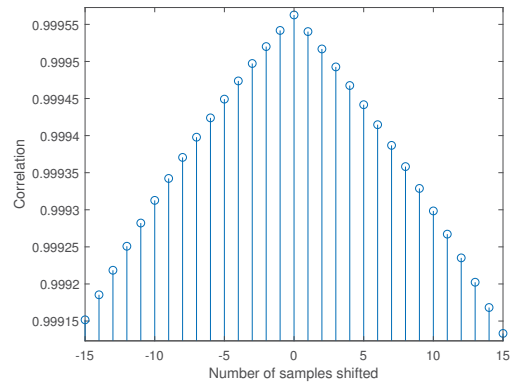


Fig. 8: Correlation of recorded signals depended on multiple shifts for mismatch determination

The limited accuracy of the scale used to weigh the cores leads to $\Delta m_{\text{core}} = \pm 0.01 \text{ g}$ and the resistance of the shunt resistor $R_{\text{shunt}} = 0.2521 \Omega$ has a tolerance of $\pm 0.2\%$.

The errors in the radii are considered as $\Delta r_{\text{in}} = \Delta r_{\text{out}} = \pm 50 \mu\text{m}$.

The signal amplitudes can be influenced by the probe's gain accuracy ($\pm 0.5\%$) and the scope. The scope's accuracy for AC signals is obtained by the frequency response of each channel with AC coupling and specified as $\pm 0.5 \text{ dB} \approx \pm 6\%$ up to the cut-off frequency of $f_{\text{cut-off}} = 1 \text{ GHz}$. Both, the DC accuracy and offset error of the scope can be calculated as $\pm 0.5\%$ of the set full scale of each channel, which varies between measurements.

Phase discrepancies $\Delta\phi_{\text{actual}}$ in this setup can be caused by the scope's sampling resolution, a mismatch between probes and the parasitic inductance of the shunt resistor. The sampling resolution results in a time delay of $\Delta t_{\text{scope}} = 50 \text{ ps}$ for the maximum sample rate of 10 GS/s . The resulting phase error can be calculated with the period T of the corresponding frequency with following equation:

$$\Delta\phi_{\text{scope}} = \frac{\Delta t_{\text{scope}}}{T} 2\pi \quad (5)$$

To specify the mismatch between the probes, a high frequency square wave signal is measured simultaneously with both probes (Fig. 7). One of the recorded signals is shifted in time by an integer number of samples ($1 \text{ S} \hat{=} 100 \text{ ps}$). For every shift the correlation of both signals is calculated. This procedure results in Fig. 8 showing a maximum correlation for no shift. Since shifting is done with the time discretization of the scope and the error caused by this time discretization has already been considered (5), the mismatch can be neglected.

The phase discrepancy caused by the inductance of the shunt $L_{\text{ESL}} \approx 35 \text{ pH}$ can be calculated with (6) by means of the angular frequency ω .

$$\Delta\phi_{\text{shunt}} = \arctan\left(\frac{\omega L_{\text{ESL}}}{R_{\text{shunt}}}\right) \quad (6)$$

With (7) and $\Delta\phi_{\text{actual}} = \pm(\Delta\phi_{\text{scope}} + \Delta\phi_{\text{shunt}})$, the overall phase error can be calculated.

$$\Delta P_{\text{Fe,dens},\phi_{\text{actual}}} = \frac{dP_{\text{Fe,dens,weight}}}{d\phi_{\text{actual}}} \Delta\phi_{\text{actual}} = -\frac{N_{\text{pri}}}{2N_{\text{sec}} R_{\text{shunt}} m_{\text{core}}} \hat{u}_{\text{shunt}} \hat{u}_{\text{sec}} \sin(\phi_{\text{actual}}) \Delta\phi_{\text{actual}} \quad (7)$$

It should be mentioned that the scope adapts the attenuation of each channel for resolutions above 100 mV/div to measure higher voltages and thereby, the time constant of the corresponding channel inevitably changes as well. However, for loss measurement it is crucial for the applied channels to be subject to the same time constant, otherwise this would result in severe errors.

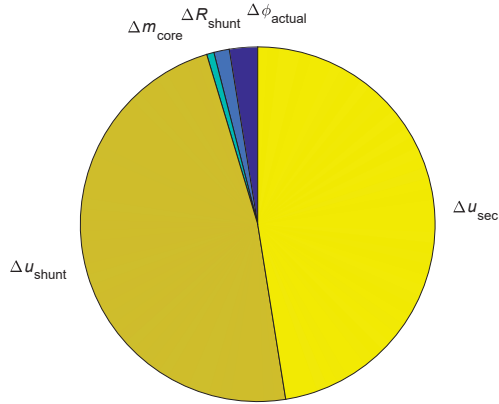


Fig. 9: Individual influences on total error of errors in phase discrepancy $\Delta\phi_{\text{actual}}$, weight Δm_{core} , value of shunt resistor ΔR_{shunt} , amplitude and offset of $u_{\text{shunt}}(t)/u_{\text{sec}}(t)$ for a typical measurement

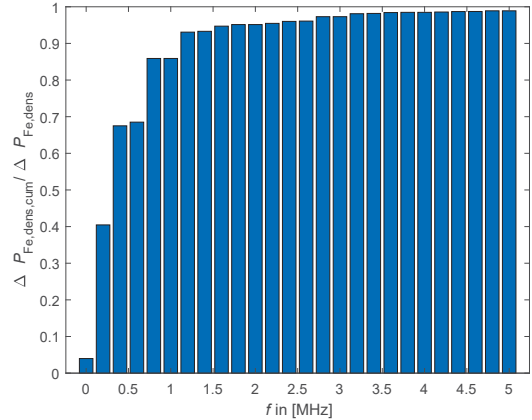


Fig. 10: Cumulative error in loss density $\Delta P_{\text{Fe},\text{dens},\text{cum}} / \Delta P_{\text{Fe},\text{dens}}$ over frequency, standardized to total error $\Delta P_{\text{Fe},\text{dens}}$, both calculated with FFT for a typical measurement

Calculation of total error

A Fast Fourier Transformation (FFT) is utilized for the total error calculation after each measurement. The resulting sinusoidal waveforms for each frequency simplify the further proceeding and allow to distinguish individual influences of all error sources and frequencies. Fig. 9 depicts the error distribution of an exemplary measurement with the cumulative loss density error over the first frequency components of the FFT in Fig. 10. It turns out that processing $u_{\text{shunt}}(t)$ and $u_{\text{sec}}(t)$ with the scope has the greatest impact on the total error. This can be explained by the scope's AC accuracy of $\pm 0.5 \text{ dB} \approx \pm 6\%$. The non-ideal DC filter deployed in the test bench leads to a small DC component of $u_{\text{shunt}}(t)$ causing the error component for $f = 0 \text{ Hz}$ in Fig. 10 with the scope's DC and offset error.

As can bee seen in Fig. 9, the error caused by discrepancies of $\Delta P_{\text{Fe},\text{dens},\phi_{\text{actual}}} / \Delta P_{\text{Fe},\text{dens}} < 3\%$ is small, although both signals measured entail very high frequencies caused by the approximately linear rising and falling current $i_{\text{pri}}(t)$. Fig. 11 shows $\Delta\phi_{\text{actual}}$ calculated by (5) - (6) and plotted up to the nyquist frequency of the scope. Despite very large phase errors for high frequencies, the influence on the total error remains relatively small due to the decreasing influence of high frequency components (Fig. 10).

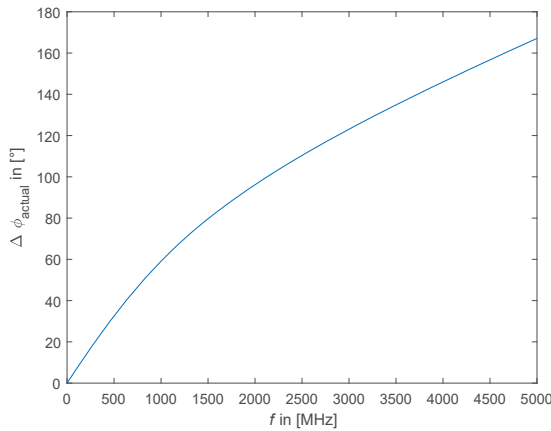


Fig. 11: Phase error $\Delta\phi_{\text{actual}}$ up to the nyquist frequency of the scope for a typical measurement

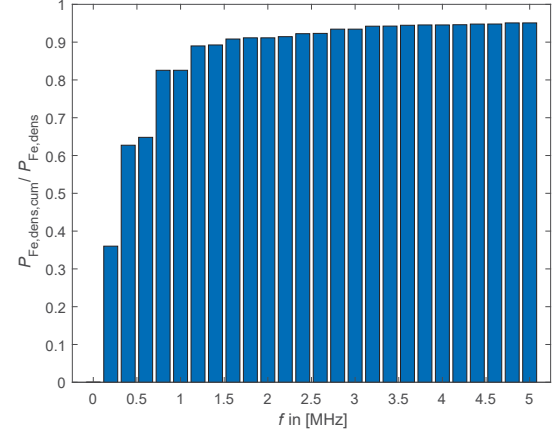


Fig. 12: Cumulative loss density $P_{\text{Fe},\text{dens},\text{cum}}$ over frequency calculated with FFT and standardized to total loss density $P_{\text{Fe},\text{dens}}$ calculated by (3) for a typical measurement

The cumulative loss density of individual frequency components normalized to the loss density derived by (3) can be seen in Fig. 12 proving that the overall loss density is mainly due to frequency components below $f < 5\text{ MHz}$ (here $> 95\%$ of losses can be explained). However, due to the nonlinear behavior of core losses mentioned above, the FFT approach isn't quantitatively accurate in calculating core losses [2] [15]. To maintain high accuracy in loss calculation, the FFT is just utilized for determining and analyzing the total error.

Depending on the waveform, the total error lies within a range of about $13\% < \Delta P_{\text{Fe,dens}} < 16\%$ for the loss density and $6\% < \Delta B_p < 9\%$ for the flux density. This is because of varying impacts of higher frequency components.

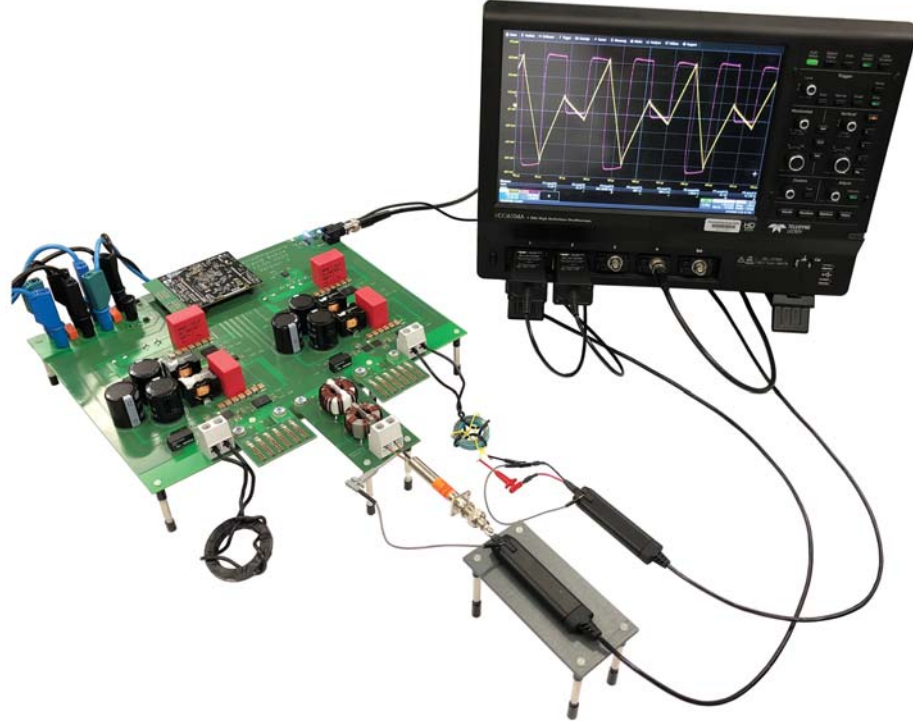


Fig. 13: Measurement setup with the scope (Lecroy HD06104A), the differential probes (Lecroy DL10-HCM), the test core (Fig. 14) and the PCB

Experimental results

First verifications of the test bench proposed are performed by determining two hysteresis curves of a nano-crystalline tape wound core based on VITROPERM®850FF [8]. All information about the test core is compiled in Table I. Other cores such as powder cores can be inserted as well.

Table I: Data of test core

inner radius	r_{in}	12.55 mm
outer radius	r_{out}	15.575 mm
width	h_{core}	6.15 mm
mass	m_{core}	10.53 g
mass density	ρ	7350 kgm ⁻³
fill factor	η	0.87156
rel. permeability	μ_r	1500
layer thickness	b_{tape}	18.183 μm



Fig. 14: test core introduced in Table I with primary and secondary side winding

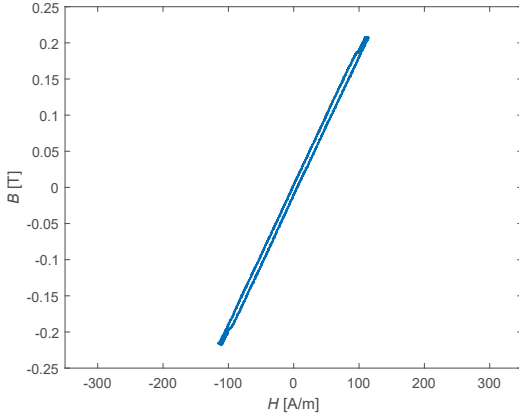


Fig. 15: Hysteresis curve of test core (Table I) for coupling path waveform with $B_p = 0.2\text{ T}$, $d = 0.3$ and $f = 100\text{ kHz}$

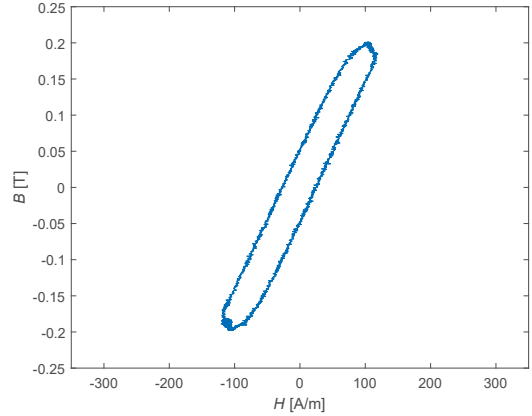


Fig. 16: Hysteresis curve of test core (Table I) for coupling path waveform with $B_p = 0.2\text{ T}$, $d = 0.3$ and $f = 700\text{ kHz}$

To avoid leakage flux in the air surrounding the core and to keep the coupling between the primary and secondary side high, windings are evenly distributed around the core (Fig. 14). This is important especially for cores with low permeability [3].

The material used has a nominal relative permeability of $\mu_r = 1500$, which corresponds to the following gradient of both hysteresis curves in Fig. 15 for $f = 100\text{ kHz}$ and in Fig. 16 for $f = 700\text{ kHz}$:

$$\mu_r = \frac{dB(t)}{dH(t)} \frac{1}{\mu_0} \approx 1500 \quad (8)$$

The small enclosed area of the B-H loop in Fig. 15 suggests very low hysteresis losses for the nano-crystalline tape material. For higher frequencies the enclosed area becomes significantly larger and with the proportionality given between the loop area and core losses, this can be directly attributed to a strong increase in losses.

There are different versions of the investigated nano-crystalline material varying in their relative permeability. As shown in Fig. 17, three cores are contrasted regarding their loss density and it can be seen, that with increasing permeability, losses slightly decrease, which was expected.

Fig. 18 shows measured loss densities $P_{\text{Fe,dens}}$ for three frequencies f over the flux density B_p , which

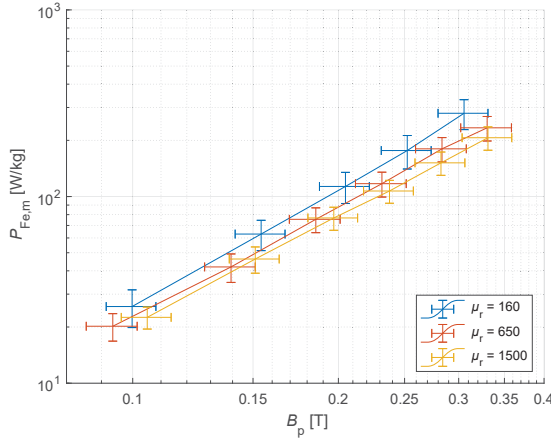


Fig. 17: Loss densities for three cores differing in their relative permeability μ_r over the flux density B_p specified for the leakage path waveform with $f = 150\text{ kHz}$, $d = 0.4$ and $k = 0.5$

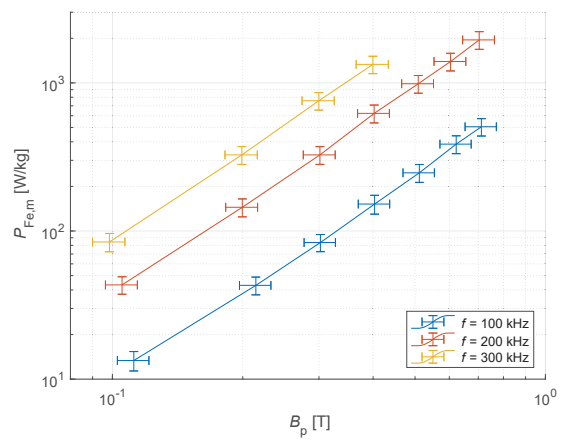


Fig. 18: Loss densities for the test core (Table I) for three different frequencies f over the flux density B_p specified for the coupling path waveform with $d = 0.3$

underlines the mentioned nonlinear dependence of core losses on both, the frequency and flux.

Core losses are proportional to $dB(t)/dt$. In order to achieve the same maximum flux B_p with smaller duty cycles, higher $dB(t)/dt$ are required. It follows that a duty cycle of $d = 0.5$ corresponds to minimal losses. As can be seen in Fig. 19, losses decrease with increasing duty cycle for $d < 0.5$ and would rise for $d > 0.5$ again.

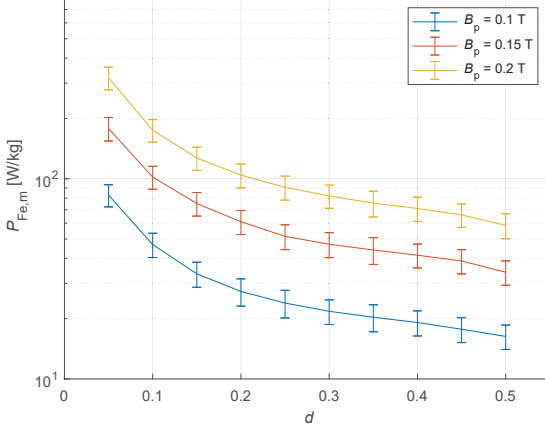


Fig. 19: Loss densities for the test core (Table I) for different duty cycles d specified for the leakage path waveform with $f = 150\text{kHz}$, $k = 0.4$ and different B_p

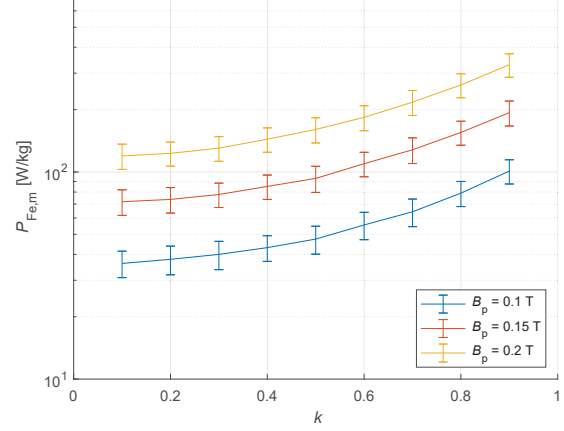


Fig. 20: Loss densities for the test core (Table I) for different coupling factors k specified for the leakage path waveform with $d = 0.3$, $f = 200\text{kHz}$ and different B_p

The total flux $B(t)$ in two-phase CI depends on the flux induced by the self inductance and on the 180° -interleaved flux induced by the coupling inductance. A high coupling factor k means a pronounced 180° -interleaved flux in the leakage path leading to higher losses (Fig. 20). The reason for that is the second harmonic of the fundamental frequency in $B(t)$ (compare Fig. 1) increasing with the coupling factor.

The leakage path waveform in Fig. 1 corresponds to triangular waveforms typically for single filter inductors in DC/DC converters for a coupling factor of $k = 0$ (compare Fig. 21). Fig. 22 depicts a comparison between loss densities measured with a coupling factor of $k = 0.4$ according to CI and $k = 0$ according to single inductors. CI show higher losses for duty cycles of $d < 0.5$ and $d > 0.5$ caused by the pronounced

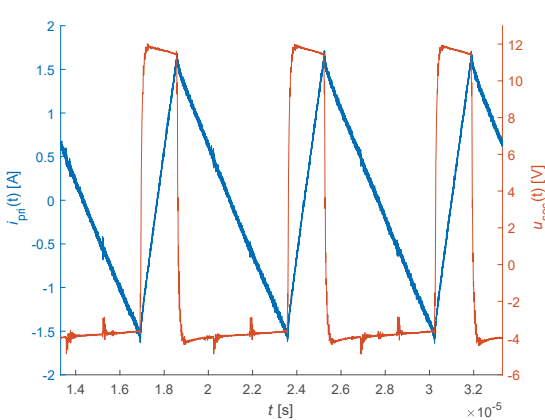


Fig. 21: Current $i_{\text{pri}}(t)$ and voltage $u_{\text{sec}}(t)$ corresponding to triangular waveforms typically for single inductors and measured for the leakage path waveform with $k = 0$, $f = 150\text{kHz}$, $B_p = 0.1\text{T}$ and $d = 0.25$

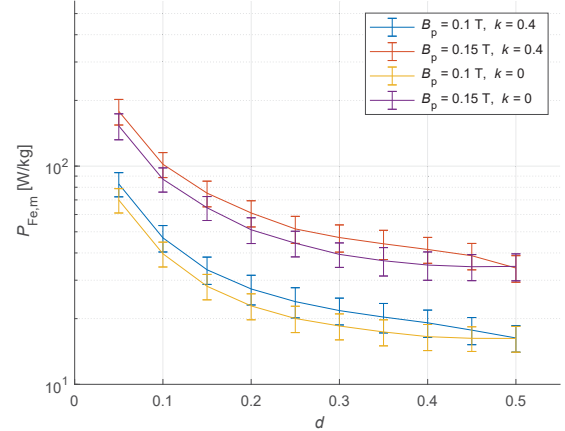


Fig. 22: Loss densities for the test core (Table I) for different duty cycles d specified for the leakage path waveform with $f = 150\text{kHz}$, different B_p and with $k = 0.4$ for CI and $k = 0$ according to single inductors

second harmonic of the fundamental frequency in $B(t)$ for $k > 0$.

With $d = 0.5$ the leakage path waveform in CI equals the triangular waveform in single inductors independent of k and so is the loss density.

Due to the automated measurement process controlled by a PC, it is possible to characterize core losses for an amount of twenty points of operation in less than 1.5 min, including error calculation for each measurement. The measurement duration varies depending on the frequency since lower frequencies require more samples per period to be processed.

Reproducing current shapes for loss measurements is crucial. For frequencies below $f < 100\text{kHz}$ large DC link capacitances with low ESL are necessary to maintain a constant DC link voltage of HB3 and HB4 in Fig. 6. The low inductance DC link capacitance deployed in this test bench is not sufficiently large to deliver such linear rising and falling current shapes (Fig. 4 and Fig. 5) at frequencies below $f < 100\text{kHz}$. Therefore, this test setup is currently limited to higher frequencies $f > 100\text{kHz}$ until the DC link capacity for HB3 and HB4 has been enlarged.

The GaN switches used, operate reliable up to frequencies $f \leq 900\text{kHz}$, which sets the upper frequency limit.

The maximum flux B_p which can be measured is dependent on the concrete core geometry but shouldn't exceed $B_p = 1\text{T}$ for the investigated material to avoid saturation.

Conclusion

The developed test bench shows good accuracy and a very high speed in measuring losses of soft magnetic materials. The automated test bench is easy to handle and fast in investigating different materials and waveforms, especially for two-phase CI.

The improvements for common mode suppression make the measurement results reliable and reproducible independent of the setup.

The low inductance DC Link capacitance needs to be enlarged for extending the frequency range for measurements to lower frequencies.

A calorimetric comparison is planned in near future.

References

- [1] P. Deck and C. P. Dick: Material savings using coupled inductors in hard switched power-electronic building blocks: Modeling and experimental validation, 2016 18th European Conference on Power Electronics and Applications (EPE'16 ECCE Europe), 2016, pp. 1-10, doi: 10.1109/EPE.2016.7695346.
- [2] M. Mu: High Frequency Magnetic Core Loss Study, Dissertation, February 2013.
- [3] A. Stadler: Messtechnische Bestimmung und Simulation der Kernverluste in weichmagnetischen Materialen, Dissertation, Erlangen, 2009
- [4] Z. Ma, J. Yao, Y. Li and S. Wang: Comparative Analysis of Magnetic Core Loss Measurement Methods with Arbitrary Excitations, 2019 IEEE Energy Conversion Congress and Exposition (ECCE), 2019, pp. 4125-4130, doi: 10.1109/ECCE.2019.8913150.
- [5] G. Herzer, V. Budinsky, C. Polak: Magnetic properties of FeCuNbSiB nanocrystallized by flash annealing under high tensile stress, 2011, physica status solidi (b) 248, doi:10.1002/pssb.201147088.
- [6] C. Jiang, X. Li, S. S. Ghosh, H. Zhao, Y. Shen and T. Long: Nanocrystalline Powder Cores for High-Power High-Frequency Power Electronics Applications, in IEEE Transactions on Power Electronics, vol. 35, no. 10, pp. 10821-10830, Oct. 2020, doi: 10.1109/TPEL.2020.2979069.
- [7] J. Petzold: Advantages of softmagnetic nanocrystalline materials for modern electronic applications, Journal of Magnetism and Magnetic Materials, Volumes 242–245, Part 1, 2002, Pages 84-89, ISSN 0304-8853
- [8] G. Herzer, V. Budinsky, C. Polak: Magnetic properties of nanocrystalline FeCuNbSiB with huge creep induced anisotropy, Journal of Physics: Conference Series, Volume 266 (2011) 012010, doi:10.1088/1742-6596/266/1/012010
- [9] F. Dong Tan, J. L. Vollin and S. M. Cuk: A practical approach for magnetic core-loss characterization, in IEEE Transactions on Power Electronics, vol. 10, no. 2, pp. 124-130, March 1995, doi: 10.1109/63.372597.
- [10] J. Muhlethaler, J. Biela, J. W. Kolar and A. Ecklebe: Core Losses Under the DC Bias Condition Based on Steinmetz Parameters, in IEEE Transactions on Power Electronics, vol. 27, no. 2, pp. 953-963, Feb. 2012, doi: 10.1109/TPEL.2011.2160971.

- [11] D. Hou, M. Mu, F. C. Lee and Q. Li: New High-Frequency Core Loss Measurement Method With Partial Cancellation Concept, in IEEE Transactions on Power Electronics, vol. 32, no. 4, pp. 2987-2994, April 2017, doi: 10.1109/TPEL.2016.2573273.
- [12] P. Y. Huang and T. Shimizu: High Power/Current Inductor Loss Measurement with Shunt Resistor Current-sensing Method, 2018 International Power Electronics Conference (IPEC-Niigata 2018 -ECCE Asia), 2018, pp. 2165-2169, doi: 10.23919/IPEC.2018.8507755.
- [13] N. F. Javidi and M. Nymand: Error analysis of high frequency core loss measurement for low-permeability low-loss magnetic cores, 2016 IEEE 2nd Annual Southern Power Electronics Conference (SPEC), 2016, doi: 10.1109/SPEC.2016.7846098
- [14] F. Schnabel and M. Jung: Calorimeter for exact determination of power losses, PCIM Europe 2019, International Exhibition and Conference for Power Electronics, Intelligent Motion, Renewable Energy and Energy Management
- [15] M. Albach, T. Durbaum and A. Brockmeyer: Calculating core losses in transformers for arbitrary magnetizing currents a comparison of different approaches, PESC Record. 27th Annual IEEE Power Electronics Specialists Conference, 1996, pp. 1463-1468 vol.2, doi: 10.1109/PESC.1996.548774.